Permeability, strength and electrochemical studies on ceramic multilayers for solid-state electrochemical cells

Andersen, Kjeld Bøhm; Charlas, Benoit; Stamate, Eugen; Kammer Hansen, Kent

Published in:
Heliyon

Link to article, DOI:
10.1016/j.heliyon.2017.e00371

Publication date:
2017

Document Version
Publisher's PDF, also known as Version of record

Heliyon

Received:
12 April 2017
Revised:
16 June 2017
Accepted:
24 July 2017

Cite as:
Kjeld Bøhm Andersen, Benoit Charlas, Eugen Stamate, Kent Kammer Hansen. Permeability, strength and electrochemical studies on ceramic multilayers for solid-state electrochemical cells. Heliyon 3 (2017) e00371.
doi: 10.1016/j.heliyon.2017.e00371

Permeability, strength and electrochemical studies on ceramic multilayers for solid-state electrochemical cells

Kjeld Bøhm Andersen, Benoit Charlas, Eugen Stamate, Kent Kammer Hansen *

Department of Energy Conversion and Storage, Technical University of Denmark, DK-4000, Roskilde, Denmark

* Corresponding author at: Department of Energy Conversion and Storage, Technical University of Denmark, Frederiksborgvej 399, DK-4000 Roskilde.

E-mail address: kkha@dtu.dk (K.K. Hansen).

Abstract

An electrochemical reactor can be used to purify flue gasses. Such a reactor can be a multilayer structure consisting of alternating layers of porous electrodes and electrolytes (a porous cell stack). In this work optimization of such a unit has been done by changing the pore former composition and the electrode powder pre-treatment. The effect on permeability, mechanical strength and electrochemical behavior was studied in this work. The effects were evaluated by measuring the pressure difference over the samples in relation to the flow through the sample, by the ball on ring method and by electrochemical impedance spectroscopy in air at temperatures between 300 and 450 °C. The resulting structures were also evaluated with scanning electron microscopy.

The work showed a dependence on the pore former composition and electrode powder pre-treatment resulting in variations in porosity, strength and flow resistance. A higher porosity gives a lower backpressure. The electrochemical performance shows that both thickness and amount of pore former in the electrolyte is important, but almost no dependence of electrode composition on the polarization resistances within the tested compositions.

Keywords: Chemical engineering, Materials science

http://dx.doi.org/10.1016/j.heliyon.2017.e00371

1. Introduction

Pollutants such as NOx emitted by the combustion of fossil fuels are a great cause of concern for the environment and for human health, and for that reason the emissions needs to be reduced. One way to lower the NOx emissions from the exhausts from i.e. diesel engines is the selective catalytic reduction of NOx with urea on a suitable catalyst [1]. This, however, requires the onboard storage of the urea and possible slip of ammonia. A potentially more convenient route for removal of NOx is to use an electrochemical reactor based on solid oxides as suggested by Pancharatnam et al. [2] and Cicero et al. [3]. In such a reactor, based on an oxide ionic conducting electrolyte, NOx is reduced at the cathode to nitrogen and oxide anions. The oxide anions are then transported through the electrolyte to the anode, where oxygen is formed. In other words electrical energy from the car battery is used directly to reduce the NOx, eliminating the need of a reducing agent.

As electrodes perovskites can be used. Perovskites of mixed oxides can have a high catalytic activity, are less expensive than noble metals, and are normally stable at higher temperatures [4].

In order to lower the space requirements of the electrochemical reactor multilayered structure with alternating layers of porous electrodes and electrodes has been suggested, see Fig. 1 [5]. This is termed a porous cell stack. The porous cell stack can be constructed from i.e. $La_{1-x}Sr_xMnO_{3+\delta}$ (a perovskite)/ $Ce_{0.9}Gd_{0.1}O_{1.95}$ composite porous electrodes and $Ce_{0.9}Gd_{0.1}O_{1.95}$ porous electrolytes [6, 7, 8, 9]. Recent studies have especially shown the necessity to increase the porosity of the membranes to lower the backpressure and improve the performance [6].

However, increasing the porosity could lower the mechanical strength of the layers [7]. The development of strong ceramic materials for purification membranes is an important aspect of the development of this technology. Ceramics failure occurs mainly due to tensile stresses, even though compressive stresses can be much higher. The mechanical tensile strength of ceramics is highly depending on the flaw distribution inside the materials. The presence of a flaw in the tensile loaded

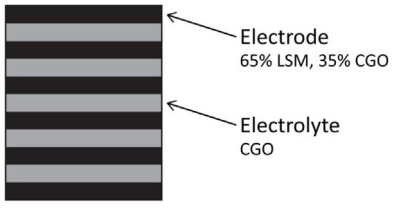

Fig. 1. Schematic presentation of the 11 layer ceramic multilayer cell with alternating layers of electrodes and electrolytes.

http://dx.doi.org/10.1016/j.heliyon.2017.e00371

volume will render the material more brittle. This is why the stress at which the material breaks is depending on the statistical flaw size and distribution inside the tested samples. The strength is therefore often described by a statistical Weibull approach determining the probability of failure of the studied materials [10, 11, 12] based on the measured failure strength of a broad number of samples.

In this study, the backpressure and mechanical strength of porous cell stacks with different set of layer thicknesses and porosities has been tested and analyzed.

The electrochemical behavior has also been analyzed using electrochemical impedance spectroscopy in air. This is done in order to evaluate the effect of changing the pore formers and starting powders on the electrochemical performance of reactors.

2. Experimental

2.1. Preparation of suspensions and tapes

The powders used in the present study were $(La_{0.85}Sr_{0.15})_{0.9}MnO_3$ (LSM) from Haldor Topsøe A/S, Denmark calcined at 800 °C and 1200 °C respectively, and $Ce_{0.9}Gd_{0.1}O_{1.95}$ (CGO) from Rhodia, France. As pore formers graphite from Alfa Aesar (plate DD50 = 2.6 μm) and polymethyl methacrylate (PMMA) micro particles from Esprix Technologies were used. Two different types of PMMA were used: Mx500 (mono dispersed with DD50 = 5 μm) and MR10 (poly dispersed with DD50 = 10 μm).

Electrode: LSM calcined at 800 °C and 1200 °C were mixed and suspended in an azeotropic mixture of methylethylketone and ethanol (MEKET). As a dispersing agent polyvinylpyrolidone (PVP) was used. The binder mixture was polyvinyl butyral (binder), polyethylene glycol and a fully acetylated glycerol monosterate, both plasticizer, in ration 1:1:1, mixed in ethanol. After ball milling for 2 days CGO and PVP were added and the suspension was ball milled for additional 24 h. Then the pore former were added and the suspension was ball milled for 5 h. Finally a binder mixture was added and the suspension was ball milled overnight. The suspension was tape casted, using a doctor blade adjusted to 0.25 mm and a casting speed of 20 cm/min.

Electrolyte: CGO, MEKET and PVP were mixed and the suspension was ball milled for 24 h. Then the pore formers were added and ball milled for 5 h. Finally a binder mixture was added and the suspension was ball milled overnight. The suspension was tape casted at a casting speed of 20 cm/min.

When the tapes were dry, the tapes were hot laminated together in an 11 layers unit with alternating layers (6 electrodes and 5 electrolytes) as described by Andersen

http://dx.doi.org/10.1016/j.heliyon.2017.e00371

et al. [6]. After lamination the samples were sintered at 1250 ° C for 4 h in a box furnace in air.

The electrodes are composed of a mixture of 65 w/w% LSM and 35 w/w% CGO, see Fig. 1. The compositions of the electrodes and electrolytes are given in Table 1 and the compositions of the 11 layers porous cell stacks are given in Table 2.

2.2. SEM samples

The sintered samples' were imbedded in epoxy and polished and the microstructures were examined using a tabletop microscope (Hitachi TM1000, Japan).

2.3. Flow resistance test

The test set up shown in Fig. 2 consists of:

- A valve for compressed air with snap connection.
- A cell house consists of 2 identical parts with grindings for O-rings. The O-rings have outer diameters of 2.5 cm and 4 cm, so the sample to be tested must have at least the same diameter or even better larger.
- Pressure difference measurement gauge that measure the pressure difference over the sample.
- Flow measurement gauge that measure the air flow through the specimen.
- A valve to control the air to the cell house.
- A stand to hold the assembled cell house.
- All the parts are assembled with tubes insuring the correct flow path and connection of the gauges.

The sample was placed in the assembled cell house. The air valve is slowly opened to apply pressure over the cell.

2.4. Experimental characterization of strength

The tapes were laminated at 130 °C and then sintered at 1250 °C for 4 h [6]. From each tape, samples were cut in discs of diameter 20 mm.

Table 1. Electrode compositions. Numbers are in weight ratio.

Name	LSM 1200	LSM 800	CGO LSA	Graphite	MR10	MX 500
LP 01	27	27	29	12	5	
LP 02	36	18	29	12		5
CP 01			77	12	11	
CP 02			74	16		10

http://dx.doi.org/10.1016/j.heliyon.2017.e00371

Table 2. The used electrodes and electrodes in the cell stacks.

Cell	Electrode	Electrolyte	Electrode casting thickness µm	Electrolyte casting thickness µm
C1	LP 01	CP 01	250	200
C3	LP 02	CP 01	250	200
C4	LP 02	CP 02	250	200
C5	LP 02	CP 02	250	100

The strength of the various layups was measured by a biaxial ball on ring flexural strength [13]

The aim of these measurements is to study the probability of failure of the different types of samples. The probability of failure of a ceramic material is given by the Weibull expression (1) [11, 12].

Type equation here

$$V_0 = \frac{1}{\sigma_{max}^m} \int_V \sum \sigma^m dV \tag{1}$$

In this expression, σ_0 is the Weibull strength and m the Weibull modulus of the material.

The set-up used in the present case has been described by other authors [13, 14]. It is a biaxial bending experiment composed of 3 main parts: the ring of radius R_r = 16 mm and section radius R_s = 2 mm, the disc (sample) of radius R_d = 10 mm and the ball of radius R_b = 2.5 mm, see Fig. 3.

The set-up was put in an Instron® press at room temperature. The load was applied by a piston on the upper ball with a constant displacement rate of 0.2 mm/min.

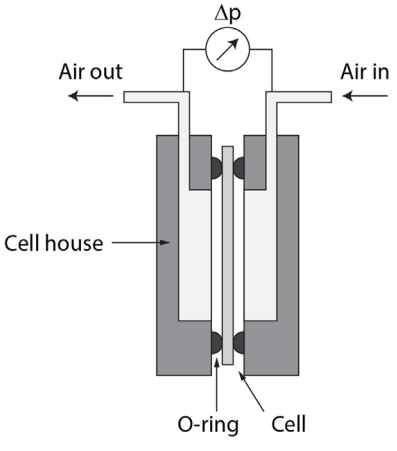

Fig. 2. Schematic model of the flow resistance test equipment.

http://dx.doi.org/10.1016/j.heliyon.2017.e00371

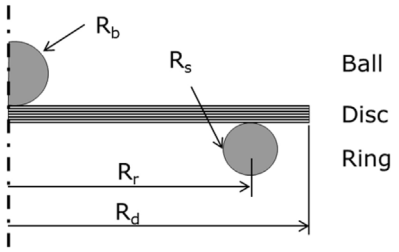

Fig. 3. Schematic of the Ball-on-Ring (BoR) set-up.

2.5. Electrochemical characterization

For the electrochemical testing, the 11 layers porous cell stacks were coated with an approximately 50 nm thick porous gold layer on both sides by sputtering. The cells were then cut into smaller samples of around 5*5 mm^2 in size. The cells were then placed between two gold meshes in a holder with space for four samples. At least two of each type of sample was tested. The holder was then placed in a furnace. Measurements were performed in air at 300, 350, 400 and 450 °C in air using a Gamry Reference 600 potentiostat. The measurements were performed from 1 MHz to 1.3 mHz with 10 points pr. decade and an amplitude of 36 mV rms. All the data were fitted using the PC windows program 'Equivalent Circuit for Windows'.

3. Results and discussion

3.1. Microstructure

The compositions of the electrodes and electrolytes are shown in Table 1. The used LSM is calcined at two different temperatures: 1200 °C and 800 °C for 2 hours, hence the names LSM1200 and LSM800. In the electrodes the LSM1200 to LSM800 ratio is changed from 1:1 to 2:1. Also the size of the PMMA pore former is changed. The electrolyte is changed by increasing the amount of pore former from 23 to 26%.

Table 2 shows the different cell stacks fabricated in this work, and Fig. 4 and Fig. 5 shows micrographs of the different cell stacks.

The SEM micrographs of the backbones showed large pores in the structure see Fig. 4. A closer look showed that there also exist many small pores, which connects the larger cavities, allowing the gas to flow through the cell without too much pressure drop.

The cell stack structure of the cell stacks, magnified 500 times (Fig. 4), showing all the layers, consisting of 6 electrodes and 5 electrolytes, giving 5 cells in series, in a porous cell stack. All porous cell stacks have well coherent structures without cracks or defects. For all cells the porosity seems uniformed distributed throughout the cell stacks. The change in PMMA pore former type is visible giving larger

http://dx.doi.org/10.1016/j.heliyon.2017.e00371

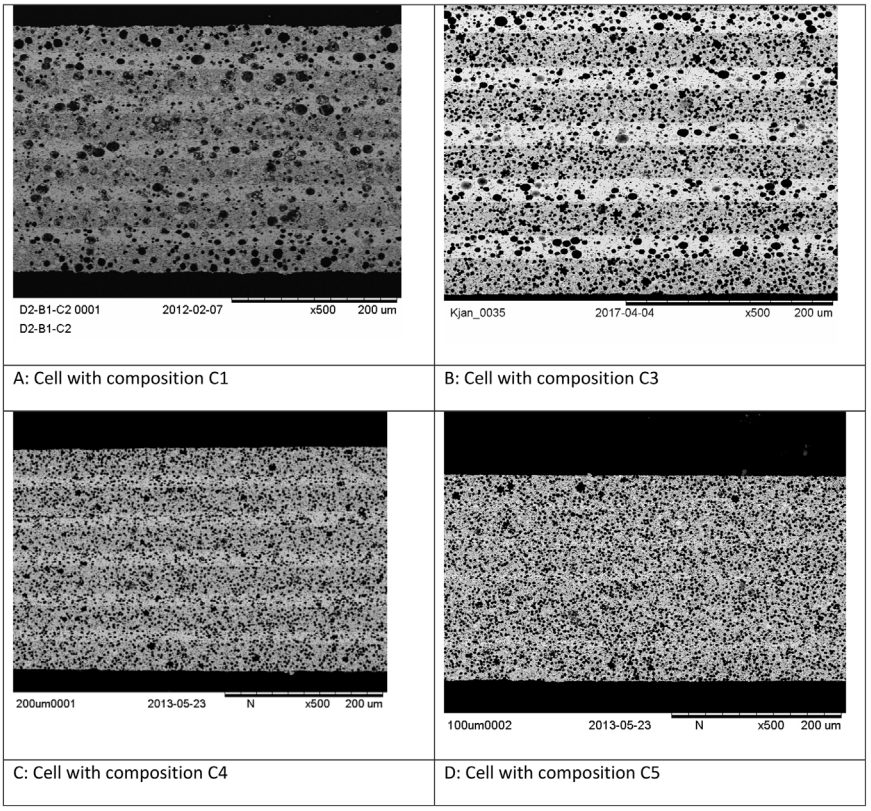

Fig. 4. 11 layer ceramic cell tested at x500 magnification. 6 electrodes and 5 electrolytes, altering between electrodes and electrolytes, with $La_{0.85}Sr_{0.15}MnO_{3}/Ce_{0.9}Gd_{0.1}O_{1.95}$ (in 65/35 weight ratio) composite porous electrodes (darker layer) and $Ce_{0.9}Gd_{0.1}O_{1.95}$ electrolyte (lighter layer). Cells with compositions A: C1, B: C3, C: C4 and D: C5 are displayed. In all SEM pictures, the altering electrode and electrolyte layers are seen. The electrode are darker then the electrolyte. The layers are clearly separated. In "A" the structure shows both smaller and larger pores, both in the electrode layer and in the electrolyte layer. In "B" only the larger pores can be seen in the electrolyte layer, where the electrode layer only have the smaller pores. The "C" sample only have the smaller pore former. In the last SEM pictures the electrolyte layer is thinner the in the former layers.

pores with PMMA MR 10, where when using PMMA MX 500, more and smaller pores are seen in the structure. Cell C1 to C4 have more or less the same thickness in the layers whereas C5 has a thinner electrolytes.

The interface between the electrode and electrolyte and the thickness of the electrolyte is also shown in Fig. 4. Also here the micrographs show that the layers are coherent and defect free. The electrodes have thickness around 30 μm, the electrolytes, casted at 200 μm, have a thickness around 20 μm and the electrode casted at 100 μm is approximate 10 μm thick. The change in composition in the electrode shows a more connected porosity when changing the LSM type ratio. In the electrodes the CGO seems well distributed in both types of electrodes.

To investigate if the LSM migrates in to the electrolyte layer, an EDS analyze of the CGO layer in C3 have been made. The result in Fig. 6 clearly shows that no

http://dx.doi.org/10.1016/j.heliyon.2017.e00371

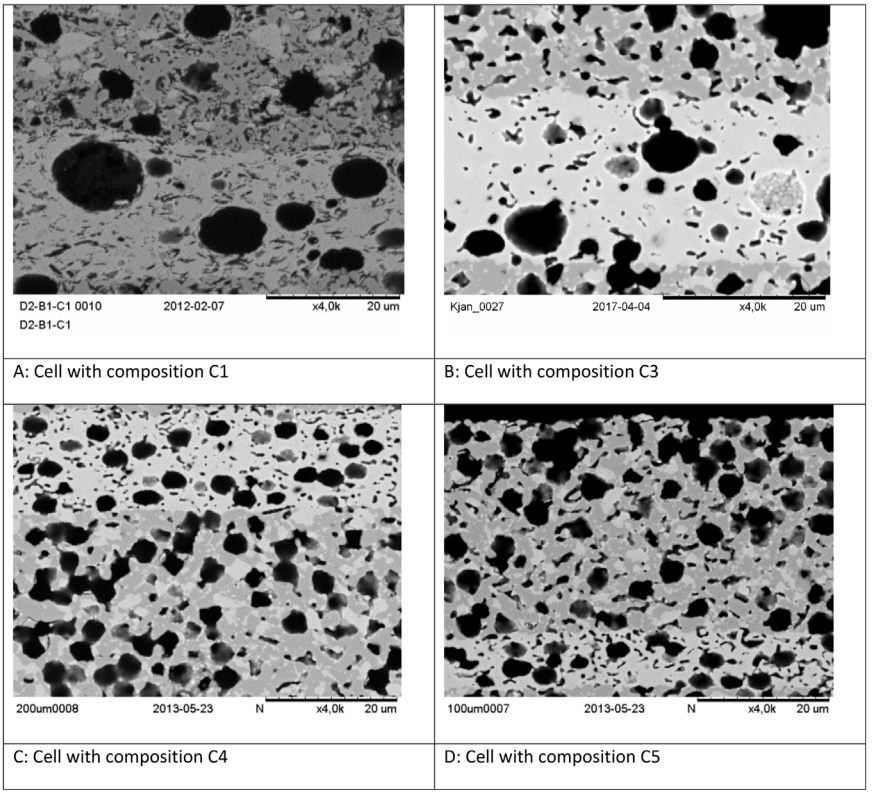

Fig. 5. 11 layer ceramic cell tested at x4000 magnification. 6 electrodes and 5 electrolytes, altering between electrodes and electrolytes, with $La_{0.85}Sr_{0.15}MnO_{3}$(LSM)/$Ce_{0.9}Gd_{0.1}O_{1.95}$ (CGO) (in 65/35%/% weight ratio) composite porous electrodes (darker layer) and $Ce_{0.9}Gd_{0.1}O_{1.95}$ electrolyte (lighter layer). Cells with compositions A: C1, B: C3, C: C4 and D: C5 are displayed. The electrode are darker then the electrolyte. The SEM pictures all shows one electrode layer and one electrolyte layer. The layers are clearly separated. In this magnification the CGO in the electrode layer is visible but no LSM is seen in the CGO layer. The CGO in the electrode layer are evenly distributed but with some agglomeration. The "A" structure have here 3 types of pore former, two round from PMMA and plate structures from Graphite pore former. The large pores are not interconnected. In structure "B" the larges pores are only seen it the electrolyte. The structure also contains the smaller round pores and the plate like pores, both in the electrode and the electrolytes. Some smaller round pores structures are connected. The SEM picture of "c" shows, that the structure only have two types of pore former. Here the pores are clearly connected. The sample in picture "D" clearly have the same structure as "C", but with a much thinner electrolyte layer. Here it is also more clear, that the electrolyte layer is uniform and coherent.

LSM is migrating in to the CGO layer. There is no La or Mn peak in the spectra and value given in Atomic percentage for La, Mn and Sr are within the uncertainty and background levels.

3.2. Backpressure of the cells

The backpressure, Table 3, from highest to lowest shown in Fig. 7 is: C1 with the electrode with LSM in the ratio 1:1 and the electrolyte with lowest porosity, C3 has a lower backpressure than C1 (the electrode is changed). When changing both the

http://dx.doi.org/10.1016/j.heliyon.2017.e00371

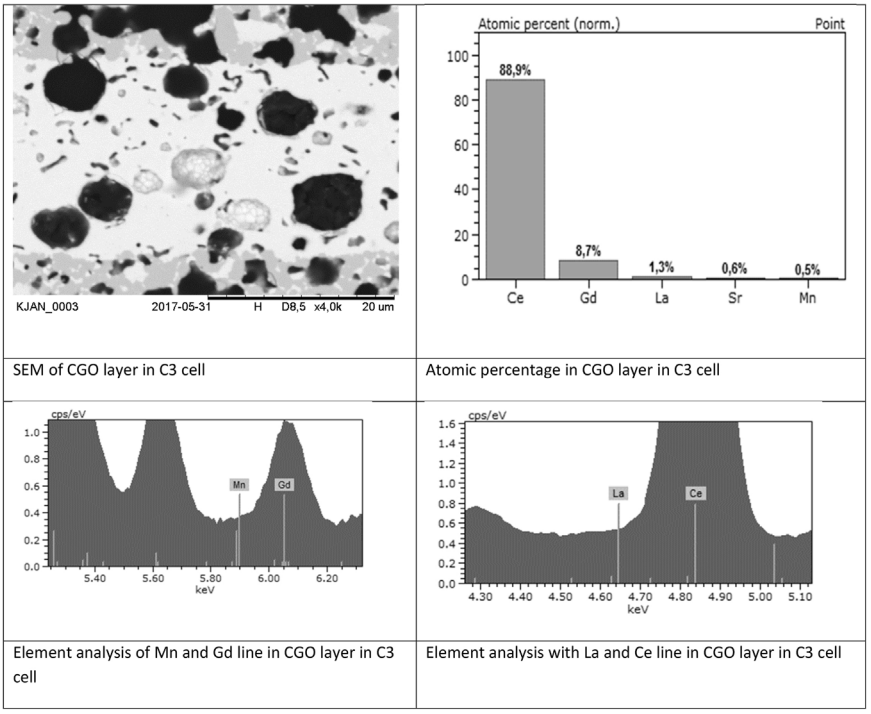

Fig. 6. EDS analysis of $\mathbf{Ce_{0.9}Gd_{0.1}O_{1.95}}$ layer in the ceramic multilayer cell.

electrode and electrolyte in C4 the backpressure gets even lower, and the cell with the lowest backpressure, C5, has the same composition as C4, but the electrolyte has approximately half the thickness.

All the curves seem to follow the same trend, that is, with increasing flow the backpressure increases. From 4 l/(min*cm^2) all the curves are linear. The backpressure decrease, when altering the compositions, are the same at all flow values. When changing the electrode, from C1 to C3, the backpressure decreases to 53% of C1. When changing the electrode and the electrolyte, from C1 to C4, the backpressure decreases to 43% of C1, and lastly when changing both the electrode and the electrolyte and decreasing the thickness of the electrolyte, form C1 to C5, the backpressure decreases to 29% of C1.

The results show that when changing the electrolyte the backpressure is decreased with 25%. Another 22% can be obtained by only changing the electrode. By changing both the electrode and the electrolyte the backpressure is reduced to less than the half showing that the backpressure over the cell stack is reduced with 57% in order to get the same flow through the cell stack. Lastly when reducing the thickness of the electrolyte in the former cell stacks the backpressure over the cell stack to get a specific flow is reduced with 71%. The tests showed that, the cell stack can be designed to have a specific flow resistance, i.e. at a flow of 4.77 l/

http://dx.doi.org/10.1016/j.heliyon.2017.e00371

Table 3. The pressure over cell at different flows for the tested cell stacks.

l/min*cm^2 Cell no.	3.18	3.98	4.77	5.57	6.37	Unit pressure difference over the cells at the flow
C1	31	34	41	48	54	mPa
C3	16	18	22	25	29	mPa
C4	13	15	18	21	23	mPa
C5	9	10	12	14	16	mPa

min*cm^2 the backpressure decreased from 41 to 12 mPa, by tailoring the electrode and electrolyte accordingly.

3.3. Mechanical properties

The elastic properties and thermal coefficient of each of the layers are necessary to analyze the stress state in the multilayer. The dependency of the elastic parameters to the porosity is expressed in the form of an exponential law (2).

$$\left(\frac{\sigma_0'}{\sigma_0}\right)^m = \frac{V_0}{V_0'} \tag{2}$$

In (2), M can either be the Young modulus E or the shear modulus G. The parameters for the calculation of the Young and shear modulus for LSM and CGO are given in Table 4 [15, 16]

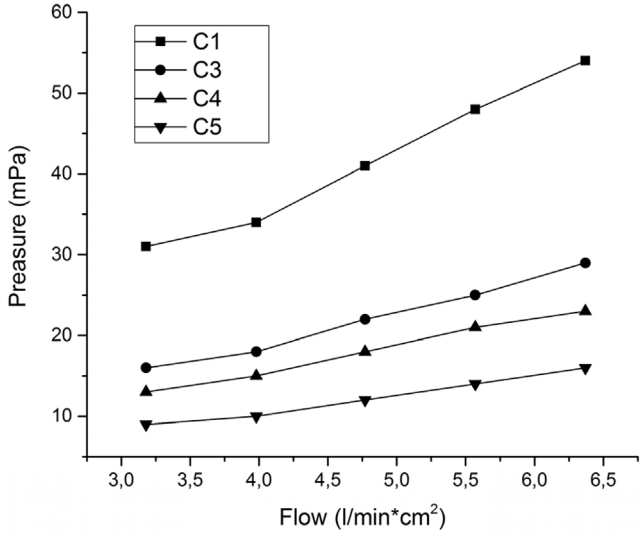

Fig. 7. Pressure-Flow curve of the tested ceramic cells. The ceramic cell is a 11 layer ceramic cell made of 6 electrodes and 5 electrolytes, altering between electrodes and electrolytes, with $La_{0.85}Sr_{0.15}MnO_3$/ $Ce_{0.9}Gd_{0.1}O_{1.95}$ (in 65/35 weight ratio) composite porous electrodes and $Ce_{0.9}Gd_{0.1}O_{1.95}$. Cells with compositions C1, C3, C4 and C5 are tested.

http://dx.doi.org/10.1016/j.heliyon.2017.e00371

Table 4. Parameter for the calculation of the porosity dependent elastic modulus E and G (2) for CGO and LSM.

	E0 (GPa)	bE	G0 (GPa)	bG	Source
LSM[1]	135.2	4.095	49.11	3.802	[15]
CGO	217.81	2.92	81.6	2.76	[16]

[1] values calculated based on the results presented in the reference publication.

The Poisson ratio is determined by (3).

$$\nu^* = \frac{E^*}{2G^*} - 1 \tag{3}$$

The thermal expansion coefficient of LSM and CGO are given in Table 5 [17, 18]

The thermo-mechanical properties of the electrodes are calculated based on the respective properties of LSM and CGO and on a theoretical mixture rule [14]. The expressions of the elastic properties are then given by (4) for the elastic properties and for the thermal expansion coefficient [19].

$$M_{MIX} = M_{CGO}V_{CGO} + M_{LSM}V_{LSM} \tag{4}$$

In (4), M can either be the Young modulus E, the shear modulus G or the bulk modulus K. α_{MIX} is the calculated thermal expansion of the mixed layer (LSM + CGO) given by (5)

$$\alpha_{MIX} = \frac{K_{CGO}\alpha_{CGO}V_{CGO} + K_{LSM}\alpha_{LSM}V_{LSM}}{K_{CGO}V_{CGO} + K_{LSM}V_{LSM}} \tag{5}$$

In (5), V_{CGO} and V_{LSM} are the respective volumetric fractions of CGO and LSM calculated considering their respective volumetric mass (respectively 7.2 and 6.5 g/cm^3) and their mass fraction M_{CGO} and M_{LSM} in the mixture (6) (7).

$$V_{CGO} = \frac{\left(\frac{M_{CGO}}{\rho_{CGO}}\right)}{\left(\frac{M_{CGO}}{\rho_{CGO}}\right) + \left(\frac{M_{LSM}}{\rho_{LSM}}\right)} \tag{6}$$

$$V_{LSM} = \frac{\left(\frac{M_{LSM}}{\rho_{LSM}}\right)}{\left(\frac{M_{CGO}}{\rho_{CGO}}\right) + \left(\frac{M_{LSM}}{\rho_{LSM}}\right)} \tag{7}$$

Table 5. Thermal expansion coefficient (TEC) of LSM and CGO.

	TEC (10–6 K-1)	Source
LSM	12.2	[17]
CGO	12.96	[18]

http://dx.doi.org/10.1016/j.heliyon.2017.e00371

Table 6. Thermo-mechanical properties of the layers in the various samples.

	E0 (GPa)	bE	G0 (GPa)	bG	TEC (10^{-6} K^{-1})
MIX	160.95	3.485	59.37	3.262	12.48
CGO	217.81	2.92	81.6	2.76	12.96

The resulting thermo-mechanical properties of the layer materials are given in Table 6

3.4. Bending strength characterization

3.4.1. Failure load

The average thicknesses (hMIX and hCGO) and porosities (pMIX and pCGO) of each layer of the four cases of tested samples are summarized in Table 7. The thickness and porosity were analyzed through image analysis.

The resulting failure forces are plotted in Fig. 8 along a Weibull distribution replacing the strength by the failure load. The corresponding Weibull load F_0 and Weibull modulus m are given in Table 8.

According to the failure load results (Fig. 8, Table 8), the repeatability of the failure load is quite remarkable for each group of samples, with a Weibull modulus m (expressing the variance of the result) ranking from 11 up to more than 14. The

Table 7. Average thicknesses (h) and porosities (p) of the electrolytes (CGO) and electrodes (MIX) layers in the various cases done by imaging analyses.

		C1		C3		C5		C4	
Layer	Material	h (µm)	P	h (µm)	p	h (µm)	p	h (µm)	p
1	**Mix**	38.89	0.44	34.07	0.46	33.77	0.50	34.82	0.47
2	**CGO**	22.84	0.36	30.37	0.54	10.37	0.44	15.80	0.34
3	**Mix**	37.35	0.44	33.09	0.41	31.85	0.45	34.32	0.41
4	**CGO**	21.30	0.35	20.74	0.29	8.40	0.42	16.30	0.32
5	**Mix**	37.96	0.43	30.86	0.41	33.33	0.44	32.35	0.39
6	**CGO**	22.84	0.32	45.93	0.52	9.26	0.43	17.28	0.32
7	**Mix**	37.96	0.43	30.86	0.41	33.33	0.44	32.35	0.39
8	**CGO**	21.30	0.35	20.74	0.29	8.40	0.42	16.30	0.32
9	**Mix**	37.35	0.44	33.09	0.41	31.85	0.45	34.32	0.41
10	**CGO**	22.84	0.36	30.37	0.54	10.37	0.44	15.80	0.34
11	**Mix**	38.89	0.44	34.07	0.46	33.77	0.50	34.82	0.47
Average on sample		339.51		344.20		244.69		284.44	

http://dx.doi.org/10.1016/j.heliyon.2017.e00371

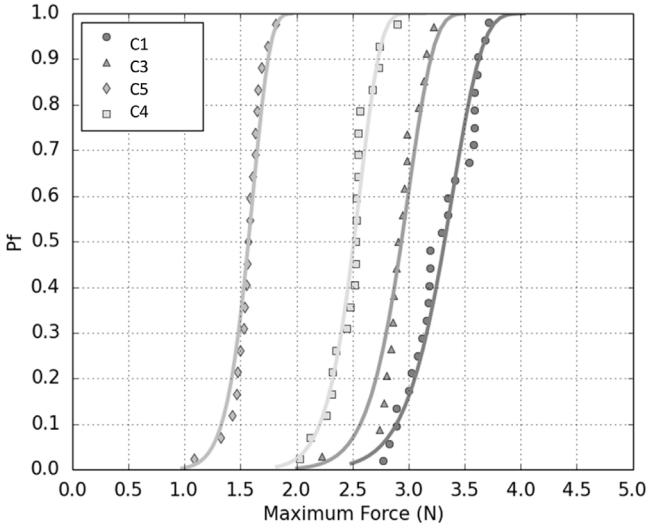

Fig. 8. Probability of failure of cells based on the breaking force of the 4 (C1, C3, C4 and C5) different compositions of ceramic cell is a 11 layer ceramic cell made of 6 electrodes and 5 electrolytes, altering between electrodes and electrolytes, with $La_{0.85}Sr_{0.15}MnO_{3}/Ce_{0.9}Gd_{0.1}O_{1.95}$ (in 65/35 weight ratio) composite porous electrodes and $Ce_{0.9}Gd_{0.1}O_{1.95}$.

highest repeatability in the failure load among the tested sample seems to be for C3 and C4 samples.

The ranking of load necessary to break the various groups of samples was (from the lowest to the highest) C5, C4, C3 and C1 samples. This ranking of failure load can partially be explained by the lower thicknesses of C5 and C4 samples compared to the others. Furthermore it does not take into account the residual thermal stresses at room temperature.

From these failure loads and taking the residual stresses into account, the strength of the lowest layer of each sample has been determined by finite element calculations.

3.5. Sample strength

In a monolayer, the failure strength is determined only by the maximum tensile stresses in the sample, which is, in the case of ball on ring, at the bottom of the

Table 8. Failing load and modulus of the Weibull distribution of the probability of failure of samples depending on the applied force.

Sample	F_0	M
C1	3.41	13.63
C3	3.01	14.13
C5	1.62	11.35
C4	2.58	14.65

http://dx.doi.org/10.1016/j.heliyon.2017.e00371

sample. In a multilayer, it is necessary to determine the failing layer, which is determined by the thermo-mechanical properties of the layer materials (which include residual stresses) and the location of the layers with respect to the mechanical loading. In the present case, the failing layer is the layer formed of mixed LSM and CGO at the bottom of the samples, even though its lower thermal expansion coefficient sets this layer under protective compressive residual stresses.

3.6. Residual stresses

The residual stresses at room temperature were determined based on thermo-elastic properties of the multilayer and on the temperature at which the elastic stresses start to build during the cooling. This reference temperature was estimated from observations of the curvature variation of a LSM/CGO bilayer during the cooling after free-sintering (Fig. 9).

The curvature seems to evolve in two times during the cooling after sintering (Fig. 9). First, at high temperature, a strong variation of curvature is generated by a small variation of temperature. This evolution can be attributed to a creep mechanism. Secondly, at lower temperature, the same amount of curvature variation can only be generated by a strong decrease of the temperature. This second evolution can be attributed to thermo-elastic properties. The transition between the two mechanisms occurs at around 1100 °C, which is taken as reference temperature for the calculation of the residual stresses.

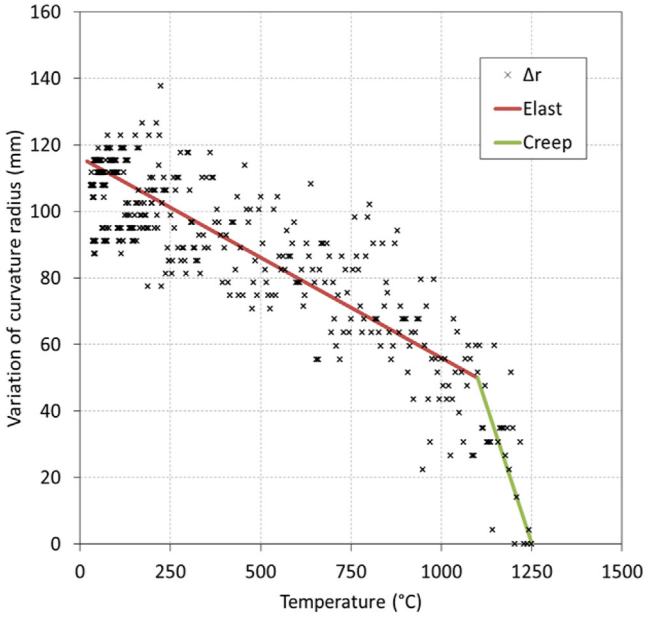

Fig. 9. Variation of curvature radius with temperature of a $La_{0.85}Sr_{0.15}MnO_{3}/Ce_{0.9}Gd_{0.1}O_{1.95}$ bilayer during the cooling after free-sintering.

http://dx.doi.org/10.1016/j.heliyon.2017.e00371

Table 9. The Table shows the correlation between the backpressure and the mechanical strength. BP is the backpressure at 5 ml/min*cm2, F0 is taken from Table 8 and T is the thickness of the samples from Table 7.

	BP/F_O	F_O/BP	BP/T	F_O/T (%)	$(FR/F_O)/T*1000$
C1	12,023	0,083	12,077	1,004	2,959
C3	7,309	0,137	6,392	0,874	2,541
C4	6,977	0,143	6,328	0,907	3,189
C5	7,407	0,135	4,904	0,662	2,706

3.7. Comparison of flow verses strength

Table 9 shows the relation between the backpressure, the strength (from the failing load) and the sample thickness. BP is the backpressure at 5 ml/min*cm^2, F_0 is taken from Table 8 and T is the thickness of the samples. The ratios between the values are calculated. For BP/F_0 and BP/T the normalized backpressure for C1 seems to have the highest value. For BP/F_0 the other samples have the same value. BP/T for C3 and C4 has an equal behavior, whereas C5 still have the lowest backpressure, when normalizing the flow/strength ratio. The normalized strength seems, with some uncertainty, to be directly dependent of the thickness. When normalizing the backpressure over the strength with the thickness, the values seems to indicate, that the ratios are the same for all the samples. So the conclusion tent to be that the value of the backpressure over strength, when the cell is normalized by the thickness, is constant.

3.8. Electrochemistry

All the data could be fitted using three (RQ) in series with a resistor, where Q is a constant phase element, see Tables 10 , 11 , 12 and 13 . For an example of a Nyquist plot see Fig. 10. It is seen that the spectrum consists of three arcs, named (going from high to low frequency) R_1, R_2 and R_3. From the results of the fitting

Table 10. Data from the fitting on C1. R is the resistance in ohm*cm2, Cw is the near equivalent capacitance in mF unless other stated and Fmax/cm2 is the summit frequency in Hz.

C1	High frequency			Medium frequency			Low frequency			
Temperature	R_1	C_ω	F_{max}	R_2	C_ω	F_{max}	R_3	C_ω	F_{max}	$R_1 + R_2 + R_3$
300 °C	1570	0.13 μ	770	916	0.013	1.3	28600	0.36	0.015	31086
350 °C	320	0.13 μ	4000	200	0.009	8.7	7098	0.27	0.084	7618
400 °C	79	0.12 μ	17000	74	0.014	15	2260	0.23	0.31	2413
450 °C	24	0.11 μ	61000	71	0.032	71	830	0.23	0.84	925

http://dx.doi.org/10.1016/j.heliyon.2017.e00371

Table 11. Data from the fitting on C3. R is the resistance in ohm*cm2, Cw is the near equivalent capacitance in mF unless other stated and Fmax/cm2 is the summit frequency in Hz.

C3	High frequency			Medium frequency			Low frequency			
Temperature	R_1	C_ω	F_{max}	R_2	C_ω	F_{max}	R_3	C_ω	F_{max}	$R_1 + R_2 + R_3$
300 °C	2130	0.14 μ	530	1180	0.013	1.0	28480	7.8	7.3e-4	31790
350 °C	480	0.14 μ	2700	338	0.012	3.9	9008	0.32	0.056	9826
400 °C	125	0.11 μ	12000	160	0.019	5.1	3265	0.28	0.18	3550
450 °C	43	0.09 μ	41000	66	0.015	16	1300	0.22	9.5	1409

the near-equivalent capacitance, C_ω, and the summit frequency, F_{max}, were calculated using equations (8) and (9) [20]:

$$C_\omega = R^{(1-n)/n} Y_0^{1/n} \tag{8}$$

$$F_{\max} = \frac{1}{2\pi}(RY_0)^{1/n} \tag{9}$$

We have previously suggested that the high frequency arc is due to transport of oxide anions from the electrode to the electrolyte, the middle frequency arc is due to transport of oxide anions in the electrode layer or adsorption of oxygen on the surface of the electrode and the low frequency arc is due to surface diffusion and bond breaking at the surface of the electrode [21, 22, 23, 24]. This is consistent with the fact that the high frequency arc is the most dependent on the electrolyte thickness (compare cells C4 and C5), and the middle frequency arc changes the less with electrolyte thickness. Also the near-equivalent capacitance for the high frequency arc is within the value for a double layer capacitance [25]. The lower total polarization resistance of the cell with the thin electrolyte compared to the

Table 12. Data from the fitting on C4. R is the resistance in ohm*cm2, Cw is the near equivalent capacitance in mF unless other stated and Fmax/cm2 is the summit frequency in Hz.

C4	High frequency			Medium frequency			Low frequency			
Temperature	R_1	C_ω	F_{max}	R_2	C_ω	F_{max}	R_3	C_ω	F_{max}	$R_1 + R_2 + R_3$
300 °C	5750	0.65 μ	430	3810	0.017	2.5	73101	0.13	0.02	82661
350 °C	1195	0.12 μ	1100	1170	0.077	1.8	18370	0.11	0.08	20735
400 °C	250	0.06 μ	10000	200	0.021	34	4469	0.08	0.46	4919
450 °C	70.7	0.06 μ	37000	83	0.034	57	1263	0.04	33	1416.7

http://dx.doi.org/10.1016/j.heliyon.2017.e00371

Table 13. Data from the fitting on C5. R is the resistance in ohm*cm2, Cw is the near equivalent capacitance in mF unless other stated and Fmax/cm2 is the summit frequency in Hz.

C5	High frequency			Medium frequency			Low frequency			
Temperature	R_1	C_ω	F_{max}	R_2	C_ω	F_{max}	R_3	C_ω	F_{max}	$R_1 + R_2 + R_3$
300 °C	1925	0.22 μ	380	2080	0·008	9.2	25300	0.14	0.045	29305
350 °C	500	0·22 μ	1500	480	0.017	19	6200	0.12	0.22	7180
400 °C	120	0.20 μ	6400	130	0.021	58	1890	0.10	0.87	2140
450 °C	36.9	0.18 μ	24000	48.2	0.024	140	800	0.08	2.4	885.1

cells with the thicker electrolyte is probably due to that more gas enters the inner electrodes of the porous cell stacks with the thin electrolyte.

There is almost no dependence of electrode composition on polarization resistances. The electrolyte with the lower amount of pore former is better conducting, as expected, and it also gives a lower total resistance probably due to more contact points between the electrode and the electrolyte (triple phase boundary).

F_{max} is decreasing with increasing temperature as expected.

The activation energies for the four resistors are given in Table 14 below. The activation energy for R_s is lower than expected for dense CGO, probably due to the porosities in the samples here used. The activation energy for R_1 is fairly constant for the four samples. The activation energy for R_2 scales with the type of electrolyte used indicating that this process occurs close to the interface. No clear trend is observed for the activation energy for R_3.

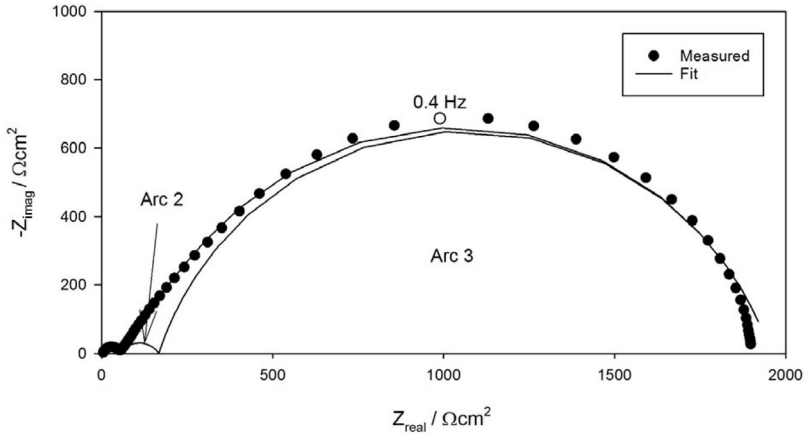

Fig. 10. Nyquist plot of recorded at 450 °C in air for the sample C5. Three arcs are seen in the spectrum. The dots are measured points and the solid line is fitted. The deconvolution of the medium and low frequency arcs are also displayed.

http://dx.doi.org/10.1016/j.heliyon.2017.e00371

Table 14. Ea values for the cell stack in eV.

	R_s	R_1	R_2	R_3
C1	0.58	0.99	0.63	0.84
C3	0.52	0.93	0.67	0.73
C4	0.60	1.05	0.94	0.97
C5	0.51	0.95	0.90	0.83

4. Conclusion

In this work, the strength of ceramic multilayer membranes for NOx reduction with solid state electrochemical cells has been tested by biaxial ball on ring flexure tests and compared. The samples are composed of 11 highly layers (6 LSM/CGO electrodes and 5CGO electrolytes) of varying thicknesses and porosities.

The failure load in such a multilayer depends on the geometrical (thickness and porosities of the layers) and on the thermo-mechanical properties of the layers (here thermo-elastic properties resulting in residual stresses). The highest failure load was reported on the thicker C1 samples. But having thick samples breaking at a high load does not necessarily mean it is a strong material. The strength of the bottom LSM/CGO layer was compared by using Weibull statistic approach on the tensile stress for each family of samples. This layer is considered to be the failing layer due to its weak mechanical properties compared to CGO.

When normalizing the backpressure over the strength with the thickness, the values seems to indicate, that the ratios are the same for all the samples. So the conclusion tent to be that the value of the backpressure over strength, when the cell is normalized by the thickness, is constant.

Even though the lowest strength could be found in the group of samples with the most porous bottom LSM/CGO layer, no clear correlation could be found between the strength of the material and the porosity of the layer. The case where this layer is the strongest is for C4 samples followed by C3 samples which are cases with intermediary porosity. However the thickness of the LSM/CGO bottom layer is pretty low (33 to 39 μm) and can therefore be influenced by the neighboring CGO layer. It seems especially that a thicker and highly porous CGO layer (C3 samples) or a thinner and less porous CGO thickness (C4) strengthens the mixed layer.

It has also been shown that the backpressure can be tailored by altering the porosity and thickness of the different layers in the porous cell stack. A thinner and more porous layer gives a lower backpressure.

http://dx.doi.org/10.1016/j.heliyon.2017.e00371

The electrochemical performance shows that both thickness and amount of pore former in the electrolyte is important. A low porosity gives a better performance, probably due to more contact points between the electrode and the electrolyte. However, a thin electrolyte layer gives a higher performance, due to more gas entering the inner electrodes. In practice it is therefore necessary to play with both porosity and thickness of layers in order to obtain a low backpressure and a high electrochemical performance.

When optimizing one parameter it has an influence on all the other parameters tested in this work. The variations in porosity influenced both low resistance, the failure load, and the electrochemical performance. For a cell with low porosity, the cell had high failure load and good electrochemical performance. The penalty was a flow resistance it high, resulting in a higher air pressure over the cell was needed to get a wanted flow. By increasing the porosity, the flow resistance decreased, but also failure load and electrochemical performance decreased. The highest porosity gave the lowest flow resistance and the lowest failure load and electrochemical performance.

In addition, the thickness of the electrolyte influenced the cell properties. The change in flow resistance and failure load can be due to a thinner cell, since the porosity does not change, but electrochemical performance gives a better performance with a thinner electrolyte.

Declarations

Author contribution statement

Kjeld Andersen: Conceived and designed the experiments; Performed the experiments; Analyzed and interpreted the data; Wrote the paper.

Kent Kammer Hansen: Performed the experiments; Analyzed and interpreted the data; Wrote the paper.

Eugen Stamate: Performed the experiments.

Benoit Charlas: Conceived and designed the experiments; Performed the experiments; Analyzed and interpreted the data.

Funding statement

This work was supported by DTU Energy.

Competing interest statement

The authors declare no conflict of interest.

http://dx.doi.org/10.1016/j.heliyon.2017.e00371

Additional information

No additional information is available for this paper

Acknowledgements

We thank the technical staff at DTU Energy for assistance.

References

[1] H. Bosch, F. Janssen, Formation and control of nitrogen oxides, Catal. Today 2 (1988) 369–379.

[2] S. Pancharatnam, R.A. Huggins, D.M. Mason, Catalytic Decompositon of Nitric oxide on Zirconia by Electrolytic Removal of Oxygen, J. Electrochem. Soc. 122 (1975) 869–875.

[3] D.C. Cicero, L.A. Jarr, Application of Ceramic Membranes in Advanced Coal-based Power-Generation Systems, Sep. Sci. Technol. 25 (1990) 1455–1472.

[4] G. Pecchi, E.J. Delgado, Perovskite: Crystallography, Chemistry and Catalytic Performance — 2013, Nova Science Publishers, Inc, USA, 2013, pp. 97–116.

[5] R.M.L. Werchmeister, K. Kammer Hansen, M.B. Mogensen, Electrochemical removal of NO_x with porous cell stacks, Mater. Research Bull. 45 (2010) 1554–1561.

[6] K.B. Andersen, F. Bræstrup, K. Kammer Hansen, Fabrication of highly porous LSM/CGO cell stacks for electrochemical flue gas purification, Ceram. Int. 39 (2013) 2159–2163.

[7] Z. He, K.B. Andersen, L. Keel, F.B. Nygaard, M. Menon, K. Kammer Hansen, Processing and Characterization of Porous Electrochemical Cells for Flue Gas Purification, Ionics (Kiel) 15 (2009) 427–431.

[8] M. Skovgaard, K.B. Andersen, K. Kammer Hansen, Pore former induced porosity in LSM/CGO cathodes for electrochemical cells for flue gas purification, Ceram. Int. 38 (2012) 1751–1754.

[9] C.G. Schmidt, D. Ippolito, J.J. Bentzen, K.B. Andersen, A. Kaiser, K. Kammer Hansen, Fabrication and Characterization of Multi-Layer Ceramics for Electrochemical Flue Gas Purification, J. Electrochem. Soc. 160 (2013) E113–E119.

[10] A. Khalili, K. Kromp, Statistical properties of Weibull estimators, J. Mater. Sci. 26 (1991) 6741–6752.

 http://dx.doi.org/10.1016/j.heliyon.2017.e00371

[11] F.P. Knudsen, Dependence of Mechanical Stength of Brittle Polycrýstalline Speciments on Porosity and Grain Size, J. Am. Ceram. Soc. 42 (1959) 376–387.

[12] W. Weibull, The phenomenon of rupture in solids, Generalstabens Litografiska Anst., 1939.

[13] H.L. Frandsen, T. Ramos, A. Faes, M. Pihlatie, K. Brodersen, Optimization of the strength of SOFC anode supports, J. Eur. Ceram. Soc. 32 (2012) 1041–1052.

[14] A. Faes, H.L. Frandsen, A. Kaiser, M. Pihlatie, Strength of Anode-Supported Solid Oxide Fuel Cells, Fuel Cells 11 (2011) 682–689.

[15] S. Giraud, J. Canel, Young's modulus of some SOFCs materials as a function of temperature, J. Eur. Ceram. Soc. 28 (2008) 77–83.

[16] A. Selcuk, A. Atkinson, Elastic properties of ceramic oxides used in solid oxide fuel cells (SOFC), J. Eur. Ceram. Soc. 17 (1997) 1523–1532.

[17] E.V. Tsipis, V.V. Kharton, Electrode materials and reaction mechanisms in solid oxide fuel cells: a brief review, J. Solid State Electrochem. 12 (2008) 1367–1391.

[18] A. Atkinson, A. Selcuk, Residual stress and fracture of laminated ceramic membranes, Acta Mater. 47 (1999) 867–874.

[19] D.K. Hale, The physical properties of composite materials, J. Mater. Sci. 11 (1976) 2105–2141.

[20] T. Jacobsen, B. Zachau-Christiansen, L. Bay, S. Skaarup, et al., High Temperature Electrochemistry: Ceramics and Metals, In: F.W. Poulsen (Ed.), Proceedings of the 17th International Symposium on Materials Science, Roskilde, Denmark, 1996, pp. 29.

[21] M. Jørgensen, M. Mogensen, Impedance of solid oxide fuel cell LSM/YSZ composite cathodes, J. Electrochem. Soc. 148 (2001) A433–A442.

[22] R. Werchmeister, K.K. Hansen, M. Mogensen, Characterisation of $La_{1-x}Sr_xMnO_3$ and doped ceria composite electrodes in NO_x containing atmosphere with impedance spectroscopy, J. Electrochem. Soc. 157 (5) (2010) P35–P42.

[23] M.L. Traulsen, K.B. Andersen, K.K. Hansen, NO_x conversion on LSM15-CGO10 cell stacks with BaO impregnation, J. Mater. Chem. 22 (2012) 11792–11800.

http://dx.doi.org/10.1016/j.heliyon.2017.e00371

[24] Z. He, K.B. Andersen, F.B. Nygaard, K.K. Hansen, A combined SEM, CV and EIS study of Multi-layered Porous Ceramic Reactors for Flue Gas Purification, Ceram. Int. 39 (2013) 847–851.

[25] S.B. Adler, J.A. Lane, B.C.H. Steele, Electrode Kinetics of Porous Mixed-Conducting Oxygen Electrodes, J. Electrochem. Soc 143 (1996) 3554.

 http://dx.doi.org/10.1016/j.heliyon.2017.e00371